Binary Neutron Star Merger Remnants as Sources of Cosmic Rays Below the "Ankle"

X. Rodrigues[a], D. Biehl[a], D. Boncioli[a], A. M. Taylor[a]

[a] *Deutsches Elektronen-Synchrotron (DESY), Platanenallee 6, D-15738 Zeuthen, Germany*

Abstract

We investigate non-thermal electron and nuclei energy losses within the binary neutron star merger remnant produced by the event GW170817. The lack of a cooling feature within the detected synchrotron emission from the source is used to constrain the magnetic field at the mG level, assuming that this emission is electron synchrotron in origin, and that the accelerated spectrum in the electrons follows the form $dN/dE_e \propto E_e^{-2}$. The level of subsequent gamma-ray emission from the source is demonstrated to provide a further constraint on the source magnetic field strength. We also put forward alternative strong ($\sim$10 G) magnetic field scenarios able to support this emission. For such stronger fields, the photo-disintegration of non-thermal nuclei within the source is considered, and a bottleneck period of $\sim$5-30 days is found when this process peaks. We find that this class of source is in principle able to support the population of cosmic rays detected at Earth below the "ankle".

Keywords: astrophysics

1. Introduction

The gravitational wave event detected on 17 August, 2017 [1] originated from the first discovered binary neutron star (BNS) merger event GW170817. Immediately following this event (within 2 s), prompt short GRB emission was detected by both Fermi-GBM and the INTEGRAL-SPI detectors [2, 3]. Subsequently, a relatively bright electromagnetic counterpart, EM170817, in optical bands was discovered [4, 5, 6, 7, 8]. This optical counterpart is associated to emission from the remnant. An estimation on the distance to the remnant from the GW signal was found to be consistent with that of the nearby galaxy NGC 4993 [9] ($\sim$40 Mpc), connecting the GW source with this host galaxy.

Subsequent non-thermal observations of the remnant in both radio and X-ray bands [10, 11] indicated that efficient in situ particle acceleration is taking place within the source. This emission was observed to brighten as a power-law in time for a timescale of ∼160 days, with the apparent recent onset of a dimming of the source [12, 13].

The outflowing kinetic energy (KE) released in the blast wave, estimated from gravitational binding energy considerations, may be of the order of 10^{50-52} erg. An estimated KE in the outflow of 10^{50} erg would be consistent with an estimated mass of 10^{-2} $M_\odot$ of material being ejected with velocity $\beta = 0.1$. At late times ($t \approx 100$ days), the estimated average density of material in the outflow is $n \approx 10^5$ cm^{-3}. Depending on the rate at which the blast wave entrains material, the non-thermal energy density in the relativistic particles, and magnetic field, may eventually rise up into closer balance with the outflowing ram-pressure ($\sim 10^{12}$ eV cm^{-3}) on the Sedov-phase timescale.

With a total mass $M = 10^{-2} M_\odot$, the total number of electrons in the outflow is $N_e = 10^{55}$. For such a massive compact outflow, two important timescales are worth noting. Firstly, the opacity of the source to its own radiation is

$$t_{e\gamma} \; = \; \frac{N_e \sigma_T R}{V} \; \approx \; \frac{N_e \, \sigma_T}{4(\beta c t)^2} \; = \; \left(\frac{t}{5 \text{ days}} \right)^{-2} . \qquad (1)$$

Thus, the early compact source would be expected to have undergone a transition from being optically thick to thin on a timescale of $t \sim 5$ days (see also [14]).

Secondly, adopting an ejecta mass of $10^{-2} M_\odot$, the Sedov phase occurs when $\langle n \rangle = M / m_p (\beta c t)^3$, giving

$$t = 3 \; \frac{0.1}{\beta} \left(\frac{10^3 \text{ cm}^{-3}}{\langle n \rangle} \right)^{1/3} \text{ yr}, \qquad (2)$$

Thus, depending on the mean ambient density that the remnant expands into ($\langle n \rangle$), the non-thermal brightening of the source could in principle occur considerably beyond the ~ 100 day timescale.

The case for late-time acceleration of particles in outflows from BNS merger events was anticipated in [15]. These authors motivated the magnetic fields to be ∼mG in strength, a shock speed of $\beta \approx 0.1$, an outflow mass of $\sim 10^{-2}$ $M_\odot$, and inferred a maximum proton energy of $\sim 10^{17}$ eV for the case of particle acceleration up to the deceleration timescale $t_{\rm dec} \approx 1$ yr, after which the outflows velocity starts to decelerate (presumed to reach the Sedov phase). Indeed, the mildly relativistic aspect of these outflows

motivates them as interesting cosmic ray (CR) acceleration sites on theoretical grounds [16]. Thus, these sources can be naturally motivated to be potential accelerators of extragalactic CRs in the "knee" to "ankle" regions of the spectrum.

Here we focus on both electron and nuclei acceleration within the source, considering the subsequent energy losses and emission. We further assess the potential interactions that accelerated nuclei may undergo within the source's radiation fields. In Sec. 2, constraints are placed on the source magnetic field under the assumption that electrons accelerated by the source posses a Fermi shock acceleration type spectrum. In Sec. 3, consideration is made on the number of non-thermal synchrotron-emitting electrons required to power the source at its observed brightness level, dependent on the source magnetic field strength, with both "low" and "high" magnetic field strength values being considered. The level of the inverse Compton (synchrotron self-Compton, SSC) emission produced for the various magnetic field strengths considered is also addressed. In Sec. 4, the subsequent interaction of non-thermal nuclei accelerated by the source, with the intense thermal radiation field observed on early (multi-day) timescales after the merger, are determined. The conclusions are made in Sec. 5. Throughout this discussion, we assume that the non-thermal emission produced on days to hundreds of day timescales is emitted isotropically by the source.

2. Magnetic Field Constraints

Photospheric velocity measurements of the remnant EM170817 provide evidence supporting the presence of an outflow with velocity $\beta \sim 0.1$ [14]. Furthermore, this outflow has been observed to give rise to non-thermal emission whose brightness has been growing with time at both radio ($\sim 0.3 - 6 \times 10^{-5}$ eV) and X-ray ($\sim 0.3 - 8 \times 10^{3}$ eV) energies [10, 11]. This emission, assumed synchrotron in origin, may be emitted by an electron population accelerated to a spectrum $dN/dE_e \propto E_e^{-2}$. The apparent lack of a cooling feature in the observed spectrum, between radio and X-ray energies, can be used to impose constraints on the synchrotron cooling rate within the source.

Dynamical time limited acceleration. The above-mentioned constraint on the minimum magnetic field strength can also be placed from a consideration of the acceleration timescale,

$$t_{\rm acc} = \left(\frac{1}{\beta^2}\right) t_{\rm Lar}, \tag{3}$$

where $t_{\rm Lar}$ is the Larmor time. For the requirement that $t_{\rm acc} < t_{\rm dyn}$, this converts to $t_{\rm Lar} < 10^{-2}\ t_{\rm dyn}$ (adopting $\beta = 0.1$).

Cooling time limited acceleration. The lack of a cooling feature in the electron spectrum can be used to place a constraint on the maximum magnetic field giving rise to the observed synchrotron emission. The synchrotron cooling time of mono-energetic electrons with Larmor radius giving rise to synchrotron photons with characteristic energy $E_\gamma^{\rm syn}$ is,

$$\begin{aligned} t_e^{\rm syn} &= \frac{9}{8\pi\alpha}\left(\frac{m_e}{E_\gamma^{\rm syn}}\right) t_{\rm Lar} \\ &= 2\times10^3\left(\frac{10\ {\rm keV}}{E_\gamma^{\rm syn}}\right) t_{\rm Lar}. \end{aligned} \tag{4}$$

Assuming the electron spectrum is produced via Fermi non-relativistic shock acceleration, giving rise to $dN/dE_e \propto E_e^{-2}$, the lack of a cooling feature in the observed synchrotron spectrum constrains the cooling time of the electrons producing this emission, $t_{\rm dyn} < t_e^{\rm syn}(E_\gamma^{\rm syn} = 10\ {\rm keV})$, leading to the constraint, $t_{\rm Lar} > 4\times10^{-4}\ t_{\rm dyn}$.

Thus, overall, a dual constraint on the Larmor period of the particles in the system is found of,

$$4\times10^{-4} < t_{\rm Lar}/t_{\rm dyn} < 10^{-2}, \tag{5}$$

where $t_{\rm dyn} \sim 100$ days $\sim 9\times10^6$ s. As a reference, it is useful to note that a 100 TeV electron in a mG magnetic field has a Larmor period of $\sim 6\times10^4$ s.

The Larmor time relates to the synchrotron photon energy emitted ($E_\gamma^{\rm syn}$) and the emitting electron energy (E_e), via the relation,

$$t_{\rm Lar} = \frac{3}{2}\left(\frac{E_e}{m_e}\right)^3\left(\frac{h}{E_\gamma^{\rm syn}}\right). \tag{6}$$

The constraint on $t_{\rm Lar}$ may therefore be expressed as a constraint on the maximum electron energy and magnetic field strength. The dynamical time limit, for which $t_{\rm Lar} = 10^{-2}\ t_{\rm dyn}$, places the acceleration energy scale at $\sim 10^{13}$ eV (and a corresponding magnetic field strength of ~ 0.1 mG). Conversely, the cooling time limit, for which $t_{\rm Lar} = 4\times10^{-4}\ t_{\rm dyn}$, places these scales at $\sim 9\times10^{12}$ eV and the magnetic field strength at a value of 2 mG. Therefore, the overall dual constraint on the magnetic field in the system is,

$$0.1\ {\rm mG} < B < 2\ {\rm mG}. \tag{7}$$

Within the inferred magnetic field strength range, the corresponding maximum energy for protons (assuming no energy losses), following the adoption of a 2 mG magnetic field throughout the age of remnant, obtained by balancing $t_{\rm acc}$ with $t_{\rm dyn}$, is

$$\begin{aligned} E_p^{\rm max} &= \beta^2 c t_{\rm dyn} B \\ &\approx 2 \times 10^{15}\ {\rm eV}. \end{aligned} \tag{8}$$

3. Non-Thermal Electron Losses

In actuality, two alternative (extreme) scenarios exist that can explain the observed luminosity of the synchrotron emission. With a low magnetic field, like that obtained above, an electron energy density is needed that far surpasses the magnetic energy density (see discussion in Sec. 3.1). However, an alternative scenario is that a high magnetic field is present (to boost synchrotron production), although this violates the constraint derived previously from the lack of a cooling feature. This violation can be negated, however, in two possible ways. Firstly, if the observed synchrotron spectrum is actually all produced by cooled electrons, injected by the source with a much harder acceleration spectrum than that produced by Fermi acceleration. Or secondly, if the synchrotron radiation is produced by protons. In the following we discuss possible parameter sets representative of either extreme magnetic field case.

3.1. Low Magnetic Field Synchrotron Emission

In this scenario, a uniform 2 mG magnetic field is considered present within the remnant. The peak of the synchrotron power emitted by an electron distribution is dominated by the highest-energy electrons accelerated. Assuming an electron synchrotron origin of the observed X-ray emission, it is dominated by electrons of energy

$$E_e^{\rm X-ray} \,=\, 10 \left(\frac{E_\gamma}{10\ {\rm keV}} \right)^{1/2} \left(\frac{B}{2\ {\rm mG}} \right)^{-1/2}\ {\rm TeV}. \tag{9}$$

In this monochromatic approximation, the total X-ray luminosity emitted by a population of electrons is

$$L_{\rm syn}^{\rm X-ray} \,\approx\, c\,\sigma_T\,(E_e^{\rm X-ray}/m_e c^2)^2\,u_B\,N_e^{\rm X-ray}, \tag{10}$$

where $N_e^{\rm X-ray}$ is the number of X-ray-emitting electrons. As a reference for the synchrotron luminosity we rely on observations around 110 days after

the event [17]. Using an approximate value of $L_{\rm syn}^{\rm X-ray} = 4 \times 10^{39}$ erg s^{-1} at 10 keV, Eq. 10 yields $N_e^{\rm X-ray} = 3 \times 10^{46}$. Since the number of non-thermal electrons goes as $E_e \frac{dN}{dE_e} \propto E_e^{-1}$, the total number of accelerated electrons is dominated by the lowest-energy, radio-emitting electrons, whose number is given by

$$N_e^{\rm radio} = N_e^{\rm X-ray} \frac{E_e^{\rm X-ray}}{E_e^{\rm radio}}. \quad (11)$$

This yields a number of MeV-electrons of 10^{53}. Thus, in this "weak" magnetic field scenario, the synchrotron-emitting electron population is rather close to the maximum possible number of swept-up and injected electrons at the Sedov phase (some $N_e^{\rm total} = 10^{55}$). This is particularly so bearing in mind that only 1% of the non-thermal particle population within sources are thought to be electrons [18]. Finally, note that in this scenario the electron energy density is much higher than the magnetic energy density, $u_e \approx 10^3 u_B$, assuming a volume of 10^{50} cm^3 corresponding to a sphere expanding with velocity $\beta = 0.1$ after 110 days.

Finally, note that the maximum energy that may be achieved by electrons in the source may be higher than that which dominates X-ray production, as shown in the left panel in Fig. 1. For $B = 2$ mG, a cooling break is expected at 10 TeV in the electron spectrum, when $t_{\rm cool} = t_{\rm dyn}$. If there is a population of cooled electrons above this energy, then they may extend up to $E_e^{\rm max} = 100$ TeV, where acceleration itself becomes limited by cooling, and a cooling cutoff occurs [19].

3.2. High Magnetic Field Synchrotron Emission

A somewhat opposite scenario involves a strong (10 G) magnetic field. Firstly we consider the case in which the X-ray luminosity is produced by lower energy electrons than in the weak magnetic field scenario, $E_e^{\rm X-ray} =$ 100 GeV (*cf.* Eq. 9). To account for the observed X-ray luminosity, the necessary number of high-energy electrons is $N_e^{\rm X-ray} = 2 \times 10^{42}$, which by Eq. 11 yields a total number of electrons of 10^{47}, which sits comfortably lower than the value derived for the "low magnetic field" scenario discussed in the previous section. In this high magnetic field scenario, however, the energy density of the non-thermal electrons and magnetic field are related by $u_e \approx 10^{-8} u_B$. As shown in the right panel of Fig. 1, the maximum electron energy allowed in this case is only 2 TeV, with synchrotron cooling dominating over acceleration at higher energies.

Alternatively, for this strong magnetic field case, the synchrotron emission may originate from a non-thermal proton population. To account for

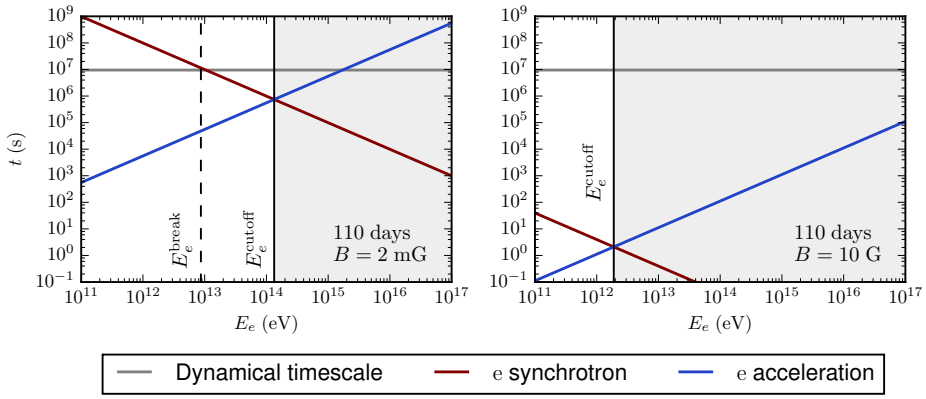

Figure 1: Relevant timescales for the case of a low (left) and high (right) magnetic field. The dynamical timescale (gray line) is given by the expansion time of the remnant, which determines the efficiency of electron acceleration (blue) and cooling (red). In the case of low $B = 2$ mG, there should be a cooling break in the electron spectrum, assuming it extends up to $E_e^{\rm max} = 100$ TeV. This is not in conflict with observations, since X-ray is emitted by electrons at lower energies ($E_e^{\rm X-ray}$). In the case of $B = 10$ G, the lack of a cooling break in the SED limits the highest electron energy to $E_e^{\rm max} \approx 2$ TeV.

the observed X-ray luminosity, the necessary number of high-energy protons can be estimated from Eq. 10, scaled by $(m_e/m_p) \approx 10^{-3.3}$ to account for the different mass of the emitting particle. In this case, $N_p^{\rm X-ray} \approx 2 \times 10^{45}$ protons with an energy of $E_p^{\rm X-ray} = 10$ PeV would be required to produce such a flux, yielding a total number of non-thermal protons of 10^{52}. In this case, the energy densities of the non-thermal protons and magnetic field are related by $u_p \approx 0.1 u_B$.

3.3. Inverse Compton Emission

A population of non-thermal particles embedded in ambient radiation fields invariably give rise to subsequent inverse Compton emission. Assuming that the observed synchrotron radiation dominates the ambient radiation field seen by the non-thermal particle population, the inverse Compton emission produced will be dominated by synchrotron self-Compton scattering (SSC). For cases in which $u_e \gg u_B$, considerable SSC emission can be expected [20].

In order to determine the inverse Compton emission at different times, a prescription for the radiation field evolutions must be adopted. The non-thermal radiation field is normalized by fixing the X-ray luminosity, obtained from observations at 9, 15 and 110 days after the merger [17], and subse-

quently extrapolating it back in time assuming a continuation of the inferred power-law evolution of the form,

$$L_{\rm X-ray} = 2 \times 10^{39}\ (t/110\ {\rm days})^{0.6}\ {\rm erg\ s^{-1}}. \qquad (12)$$

At early times, $t < 15$ d, a bump is observed in the optical range of the SED, with a spectral shape characteristic of thermal emission [17]. This thermal bump is seen to decrease between 10 and 74 days after the event [21]. Based on these observations, we model the evolution of this thermal luminosity as

$$\begin{aligned} L_{\rm th} &= 4 \times 10^{40}\ {\rm erg\ s^{-1}} && (t <\ 7\ {\rm days}) \\ &= 4 \times 10^{40}\ (t/7\ {\rm days})^{-2.3}\ {\rm erg\ s^{-1}} && (t > 7\ {\rm days}), \end{aligned} \qquad (13)$$

(see red solid curves in Fig. 2).

In Fig. 2 we show the resultant broadband SED produced by the remnant at 5 and 110 days after the merger. Two different results are shown, to cover the uncertainty in the maximum electron energy: the spectra that peak at lower energies (solid curves) correspond to $E_e^{\rm max} = E_e^{\rm X-ray}$, while the dashed curves are obtained assuming that electrons are accelerated up to the maximum energy allowed by the cooling process (see Fig. 1), as discussed previously. The low-energy cut-on of the synchrotron spectra is given by synchrotron self-absorption, which is included in our emission model, following the prescription provided in [22].

In the top-left panel of Fig. 2 we show the case where a 30 mG magnetic field is present within the outflow at 5 days after the merger event. At these early times in the remnant, the thermal radiation field provides the dominant target for inverse Compton emission. We also show the H.E.S.S. upper limit, in the range 0.5-6 TeV, at 5.2 days [23]. The magnetic field at these early timescales has been adopted sufficiently high so as to ensure that the inverse Compton emission does not overshoot the H.E.S.S. upper limit. For this case, a sharp cutoff is introduced into the inverse Compton spectrum. This cutoff is due to pair production on the thermal radiation field, which we include in our emission model following the prescription of [24]. We note that following pair production within the source, subsequent cascade development and emission would result, leading to the redistribution of the spectrum at lower energies. However, for the purposes of comparing the inverse Compton flux to the H.E.S.S. observation upper limit, this additional lower-energy component may be neglected. The considerable level of inverse Compton emission found for the case of low magnetic field demonstrates that at later times, once the thermal bump has reduced sufficiently, a lower limit

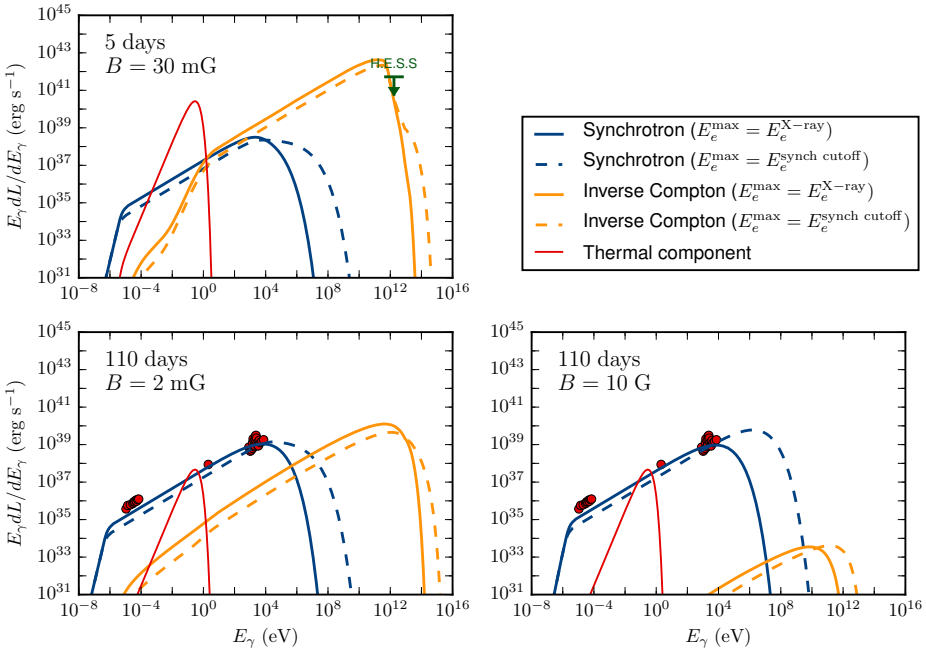

Figure 2: Luminosity spectrum produced by electron synchrotron emission (blue, including synchrotron self-absorption), and inverse-Compton scattering (yellow), at five days (top) and 110 days (bottom) after the merger event. For the 110 day case we show the results for the weak (left) and strong (right) B-field scenarios. The dashed curves are obtained if the electrons extend to the highest energies allowed (*cf.* Fig. 1), whereas the solid curves correspond to the more conservative assumption that synchrotron emission cuts off right above the observed X-rays. The limit on the TeV luminosity at 5 days (green) and the radio-to-X-ray data at 110 days (red) are observational results [23, 17].

on the magnetic field strength may be placed at late timescales, by follow-up TeV observations of the remnant.

In the bottom panels of Fig. 2 we show the resultant broadband SED produced by the remnant at 110 days, normalized to the observed X-ray luminosity for both the low and high magnetic field strength cases. At this later time in the remnant, the synchrotron radiation field provides the dominant target for inverse Compton emission. The red points in this plot show the radio, optical, and X-ray data points taken at this time [17]. For the weak magnetic field scenario result ($B = 2$ mG, bottom-left panel of Fig. 2), the inverse Compton luminosity dominance is highest and the predicted gamma-ray luminosity is 5×10^{41} erg s^{-1}, peaking at $E_\gamma = 100$ GeV. For the case of $B = 10$ G (bottom-right panel of Fig. 2), on the other hand, the

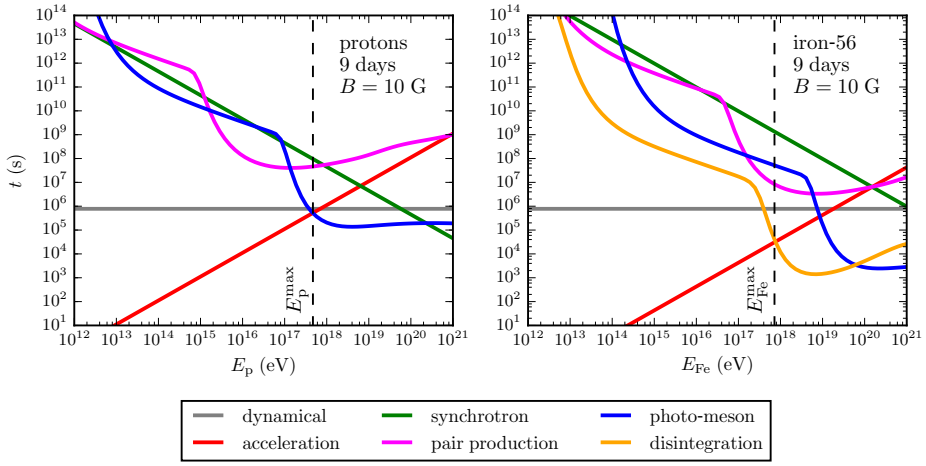

Figure 3: Interaction times for protons (left) and iron-56 nuclei (right) as a function of the particle energy, 9 days after the merger, in the high magnetic field scenario. Note that for the the synchrotron and pair production processes we show the energy loss timescale.

low electron density and maximum electron energy yield a gamma-ray power of only 10^{36} erg s^{-1} with a 10 GeV cutoff. This result demonstrates that the potential probing of the Compton peak by TeV instruments can provide fresh insights to discriminate between the different magnetic field strengths considered. Indeed, the upper limit level already placed by H.E.S.S. observations of the remnant on 5 day timescales [23] indicate that this instrument has the required sensitivity to provide such a probe, should subsequent observations be made on longer timescales.

4. Non-Thermal Nuclei Losses

Nuclei accelerated by the source will also interact with the target photons present within it. The determination of the interaction processes which dictate the maximum energy of the accelerated nuclei depends on the magnetic field strength adopted. Since the low magnetic field value discussed in Sec. 3.1 would increase the acceleration time, acceleration up to high energies and the onset of nuclear photo-disintegration would not be possible. For the purpose of investigating these interactions, we adopt in the following the high magnetic field scenario discussed in Sec. 3.2, making use of the technology of the NeuCosmA code, which has been previously developed for the cases of Gamma-Ray Bursts [25] and blazars [26].

As time proceeds, the thermal component decreases and the non-thermal part of the SED increases (see Eqs. 12 and 13). However, in terms of the photo-disintegration of CR nuclei within the source, the brightening of the non-thermal component does not compensate for the dimming of the thermal component, since the dimming of the black body spectrum is much faster than the brightening of the non-thermal emission. Since we assume a constant magnetic field, the acceleration and synchrotron loss rates do not change. Contrary to this, photo-hadronic interactions and the size of the region evolve with the expanding volume of the object. In fact, the appreciable attenuation at early times (< 10 days) of TeV photons in the source found in Sec. 3.3 gives reason to expect also considerable photo-disintegration in the source on these timescales [27, 28, 29].

We show in Fig. 3 the interaction timescales of the different processes at work for both protons (left panel) and iron-56 nuclei (right panel). As a reference, we take the time interval of 9 days after the merger, since photo-disintegration of iron-56 is found to be optimally efficient at this timescale. We also plot the pair production loss time, showing that although it is always a sub-dominant energy loss process for hadrons, it will contribute appreciably to the electron population. We can see that at the 9 day timescale the maximum energy achieved by iron-56 nuclei is 1 PeV, the energy at which photo-disintegration becomes more efficient than acceleration and the nuclei are no longer efficiently accelerated, instead producing lighter isotopes. The maximum proton energy, on the other hand, can be seen to be limited by photo-meson production. At later times, when the thermal photon luminosity decreases, both nuclear photo-disintegration and photo-meson production by protons become less efficient, and the maximum energy is limited only by the remnant age. This is represented by the dynamical timescale, $t_{\rm dyn} \sim R/(\beta c)$. Assuming continuous injection, the late time acceleration of protons (nuclei) can bring them up to energies up to (beyond) the "ankle". However, depending on the period of efficient photo-disintegration and on the primary isotope, the composition of the CRs eventually escaping the source can be quite different. As the present study is held very general, we do not make an effort to calculate the resultant late-time accelerated nuclei spectra in this work.

Since both the photon density and source size vary with time, a complete picture requires consideration of the evolution of the interaction times within the source. In Fig. 4 we show the temporal evolution of the optical depth of the source to photo-disintegration of different isotopes and photo-meson production by protons. Here, the optical depth is defined as $\tau_{\rm int} = t_{\rm dyn}/t_{\rm int}|_{\rm E_{max}}$, where $t_{\rm dyn}$ is the dynamical timescale and $t_{\rm int}$ the inter-

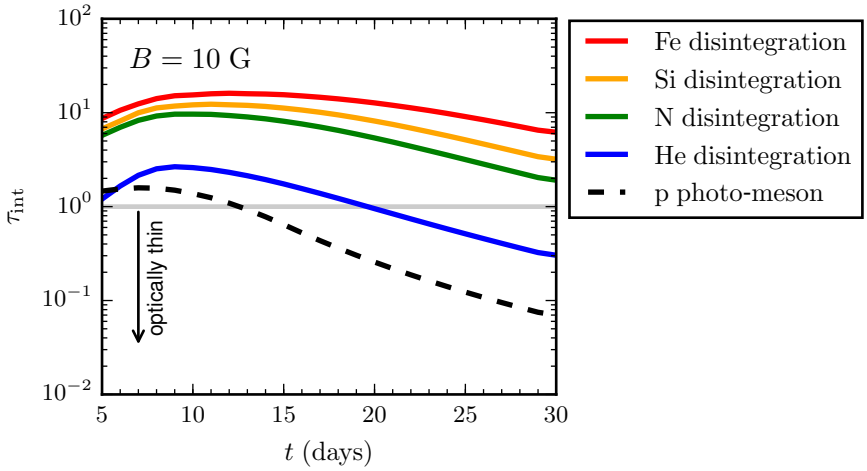

Figure 4: Optical depth of the remnant to photo-disintegration of different isotopes (solid curves) and photo-meson production by protons (dashed curve) as a function of the time since the merger, in the high magnetic field scenario. The horizontal gray line represents the transition from optically thin to thick (see main text).

action timescale, evaluated at the maximum energy of the CR (see vertical dashed line in Fig. 3). This provides a measure for whether CRs accelerated by the source rather escape from it or photo-disintegrate within it. The optimal time for nuclear photo-disintegration is found to be reached within the first weeks after the merger. This happens because of the competing processes within the expanding object, namely the rise of the maximum particle energies achievable and the decrease of the thermal component.

With some level of photo-meson production and photo-disintegration expected within the source during early times, and ultra-high energies becoming within reach at later times, we next turn our attention to the ensemble population of such sources. We implicitly assume here that the event we discuss throughout this work is representative of a population of identical sources which could accelerate CR nuclei. In this scenario, there should be a number of electromagnetic counterparts to this population, with the event EM170817 being the only one detected so far.

We focus on the local injection rate of energy needed to power the CR flux at Earth in a broad energy range. The energy range of interest is determined by the maximum energy $E_{\rm max}$ that can be achieved by the source during its evolution, and on the interaction processes involved. We use the compilation of measurements taken from several experiments as done in [30], to derive

the emissivity

$$\mathcal{L}_0 = \mathcal{L}(z=0) \;=\; 4\pi \int_{E_1}^{E_2} \frac{\phi(E, z=0)}{\lambda(E, z=0)} E dE, \tag{14}$$

where ϕ is the flux at Earth as usually given by CR experiments (in units of $1/(\text{energy} \times \text{length}^2 \times \text{solid angle} \times \text{time})$) and λ is the interaction length of the proton for the propagation through the cosmic microwave background (CMB). If we use $[E_1, E_2] = [10^{18}, 10^{19}]$ eV for the observed CR spectrum, the corresponding luminosity density for CRs is $\mathcal{L}_0 \sim 2.8 \times 10^{44}$ erg yr^{-1} Mpc^{-3}; note that the usual luminosity density which is taken as a reference from [31] is calculated at a higher energy range, which is not within the reach of the CR accelerator studied in this work.

An estimate of the required energy input into CRs in each BNS merger event in order to support the observed CR flux gives

$$E_{\rm CR} \;=\; \frac{\mathcal{L}_0}{\dot{n}} \approx 2 \times 10^{50}\,{\rm erg}, \tag{15}$$

where $\dot{n} = 1540^{+3200}_{-1220}$ Gpc^{-3} yr^{-1} is the inferred local rate of BNS mergers [1]. It is important to note that the equation above refers to the emitted CRs from the source, while the total energy input in CRs is computed by taking into account the accelerated spectrum in the source. In order to take into account the interactions in the source and the escape mechanism, an energy loss correction has to be applied to Eq. 15. Moreover, since a limited energy range $[E_1, E_2]$ is considered, an additional bolometric correction has also to be applied.

Taking into account the latest measurements reported in [32], at the timescale of 160 days after the merger event, the luminosity of the non-thermal component is 3.2×10^{41} erg s^{-1} at late times, with a corresponding integrated non-thermal energy output of 4.5×10^{48} erg. At this late timescale the hadronic processes discussed are no longer at work and the maximum energy is determined by the dynamical timescale, allowing the acceleration up to the "ankle", or beyond in the case of nuclei. We note that the derived total energy in CRs produced by a single BNS merger remnant, $E_{\rm CR}$, is roughly consistent with a fraction (10%) of the released outflowing KE estimate in Sec. 1.

With an estimated average source power of $E_{\rm CR}/t_{160\ {\rm d}} \approx 10^{43}$ erg s^{-1}, an estimate of the total neutrino fluence produced by the source can be made. Such an estimate requires knowledge of the duration of the period when the source presents a thick target to photo-meson energy losses, which

may be estimated using the results in Fig. 4. Following this, the effective period for which the source presents a thick target to photo-meson cooling is $K_{p\gamma}\Delta t_{p\gamma} \approx 1$ day, where $K_{p\gamma} \approx 0.15$ describes the fraction of energy taken by a pion in each photo-meson production interaction. The resulting estimate of the neutrino flux from the source is $E_{\rm CR}K_{p\gamma}\Delta t_{p\gamma}/(4\pi d^2 t_{160\ \rm d}) \approx 4 \times 10^{-3}$ GeV cm^{-2}, where d is the distance to the remnant. Note that the estimate of the energy input in CRs provides a normalization factor for the neutrino flux. It should, however, be kept in mind that this estimate carries considerable uncertainty, particularly due to the present large uncertainty on the source rate. However, a simple comparison with the present upper limits for neutrino flux from EM170817 [33] indicates that the level of this flux would be challenging to reach by present instruments like IceCube. For comparison, the case of neutrino emission from the BNS merger pulsar remnant was considered in [34, 35]. In both cases, rather increased neutrino fluxes were found to be expected compared to those determined here, due to the faster acceleration process at play in this source and the differing source environment.

5. Conclusion

Under the premise that the observed non-thermal emission from the remnant is isotropic, we consider the non-thermal particle energy losses within the fast-moving remnant outflow associated with EM170817 . Assuming that this emission is electron in origin, the consideration of the lack of a cooling break in the synchrotron emission from this remnant, whose age is accurately known, allowed a constraint to be made on the strength of the source magnetic field at the mG level. The subsequent synchrotron self-Compton emission expected demonstrated that for such a magnetic field strength level, large inverse Compton emission is expected. Should this component not be detected, this weak magnetic field scenario would become disfavoured.

An alternative strong magnetic field scenario was also put forward, in which two potential origins of the synchrotron emission are discussed. The first is that it is produced by electrons with a hard injection spectrum, which subsequently cool to an E^{-2} distribution. In the most extreme version of this scenario observationally allowed, magnetic fields of 10 G can be present within the source. Stronger magnetic fields than this are disallowed due to synchrotron self-absorption constraints. The second is that this synchrotron emission is produced by protons accelerated to high energies by the source.

Within the scenario of the strong magnetic field, we also tested the efficiency of photo-meson production and photo-disintegration of CRs. The

thermal component was demonstrated to be crucial for the interactions of the CRs in the outflow of the BNS merger remnant, especially at early times, when it provides the dominant target radiation field for these processes, which subsequently defines the maximum CR energy. Later, when the volume of the object has expanded, the thermal component becomes dimmer and the system is optically thin to hadronic interactions. At this point the maximum energy of protons (nuclei) is no longer dictated by losses on this thermal radiation, allowing the acceleration up to energies at (beyond) the "ankle". In order for such a population to power the observed CR flux, a total energy output in CRs by the source of $\sim 10^{50}$ erg at late timescales.

An origin of CRs below the "ankle" related to NS merger remnants carries similarities with that put forward previously by others [36, 37, 38, 39, 40, 25]. Indeed, such a scenario rather naturally explains the apparent lightness of the CR composition inferred at these energies from elongation rate measurements by the Pierre Auger Observatory [41]. The recent in-depth observations of such a remnant, over a broad energy range, have shed fresh light on the non-thermal aspects of this phenomenon, and continues to motivate them as promising CR sources.

Acknowledgements

We thank Martin Pohl, Walter Winter, and Stefan Ohm for useful discussions. This work has been supported by the European Research Council (ERC) under the European Union's Horizon 2020 research and innovation programme (Grant No. 646623).

References

[1] B. Abbott, et al., GW170817: Observation of Gravitational Waves from a Binary Neutron Star Inspiral, Phys. Rev. Lett. 119 (16) (2017) 161101. arXiv:1710.05832, doi:10.1103/PhysRevLett.119.161101.

[2] B. P. Abbott, et al., Gravitational Waves and Gamma-rays from a Binary Neutron Star Merger: GW170817 and GRB 170817A, Astrophys. J. 848 (2) (2017) L13. arXiv:1710.05834, doi:10.3847/2041-8213/aa920c.

[3] V. Savchenko, et al., INTEGRAL Detection of the First Prompt Gamma-Ray Signal Coincident with the Gravitational-wave Event

GW170817, Astrophys. J. 848 (2) (2017) L15. arXiv:1710.05449, doi:10.3847/2041-8213/aa8f94.

[4] I. Arcavi, et al., Energetic eruptions leading to a peculiar hydrogen-rich explosion of a massive star (2017). arXiv:1711.02671, doi:10.1038/nature24030.

[5] D. A. Coulter, et al., Swope Supernova Survey 2017a (SSS17a), the Optical Counterpart to a Gravitational Wave Source, Science[Science358,1556(2017)]. arXiv:1710.05452, doi:10.1126/science.aap9811.

[6] V. M. Lipunov, et al., MASTER Optical Detection of the First LIGO/Virgo Neutron Star Binary Merger GW170817, Astrophys. J. 850 (1) (2017) L1. arXiv:1710.05461, doi:10.3847/2041-8213/aa92c0.

[7] M. Soares-Santos, et al., The Electromagnetic Counterpart of the Binary Neutron Star Merger LIGO/Virgo GW170817. I. Discovery of the Optical Counterpart Using the Dark Energy Camera, Astrophys. J. 848 (2) (2017) L16. arXiv:1710.05459, doi:10.3847/2041-8213/aa9059.

[8] S. Valenti, D. J. Sand, S. Yang, E. Cappellaro, L. Tartaglia, A. Corsi, S. W. Jha, D. E. Reichart, J. Haislip, V. Kouprianov, The discovery of the electromagnetic counterpart of GW170817: kilonova AT 2017gfo/DLT17ck, Astrophys. J. 848 (2) (2017) L24. arXiv:1710.05854, doi:10.3847/2041-8213/aa8edf.

[9] J. Hjorth, A. J. Levan, N. R. Tanvir, J. D. Lyman, R. Wojtak, S. L. Schrøder, I. Mandel, C. Gall, S. H. Bruun, The Distance to NGC 4993: The Host Galaxy of the Gravitational-wave Event GW170817, Astrophys. J. 848 (2) (2017) L31. arXiv:1710.05856, doi:10.3847/2041-8213/aa9110.

[10] K. P. Mooley, et al., A mildly relativistic wide-angle outflow in the neutron star merger GW170817, Nature 554 (2018) 207. arXiv:1711.11573, doi:10.1038/nature25452.

[11] J. J. Ruan, M. Nynka, D. Haggard, V. Kalogera, P. Evans, Brightening X-Ray Emission from GW170817/GRB 170817A: Further Evidence for an Outflow, Astrophys. J. 853 (1) (2018) L4. arXiv:1712.02809, doi:10.3847/2041-8213/aaa4f3.

[12] P. D'Avanzo, et al., The evolution of the X-ray afterglow emission of GW 170817 / GRB 170817A in XMM-Newton observations, Astron. Astrophys. 613 (2018) L1. arXiv:1801.06164, doi:10.1051/0004-6361/201832664.

[13] M. Nynka, J. J. Ruan, D. Haggard, Fading of the X-ray Afterglow of Neutron Star Merger GW170817/GRB170817A at 260 days (2018). arXiv:1805.04093.

[14] A. L. Piro, J. A. Kollmeier, Evidence for Cocoon Emission from the Early Light Curve of SSS17a, Astrophys. J. 855 (2) (2018) 103. arXiv:1710.05822, doi:10.3847/1538-4357/aaaab3.

[15] H. Takami, K. Kyutoku, K. Ioka, High-Energy Radiation from Remnants of Neutron Star Binary Mergers, Phys. Rev. D89 (6) (2014) 063006. arXiv:1307.6805, doi:10.1103/PhysRevD.89.063006.

[16] A. R. Bell, A. T. Araudo, J. H. Matthews, K. M. Blundell, Cosmic Ray Acceleration by Relativistic Shocks: Limits and Estimates, Mon. Not. Roy. Astron. Soc. 473 (2) (2018) 2364–2371. arXiv:1709.07793, doi:10.1093/mnras/stx2485.

[17] R. Margutti, et al., The Electromagnetic Counterpart of the Binary Neutron Star Merger LIGO/VIRGO GW170817. V. Rising X-ray Emission from an Off-Axis Jet, Astrophys. J. 848 (2) (2017) L20. arXiv:1710.05431, doi:10.3847/2041-8213/aa9057.

[18] G. R. Burbidge, Estimates of the total energy in particles and magnetic field in the non-thermal radio source, Astrophys. J. 129. doi:10.1086/146680.

[19] F. A. Aharonian, TeV gamma-rays from BL Lac objects due to synchrotron radiation of extremely high-energy protons, New Astron. 5 (2000) 377–395. arXiv:astro-ph/0003159, doi:10.1016/S1384-1076(00)00039-7.

[20] C. Fransson, C.-I. Björnsson, Modeling the radio and x-ray emission of SN 1993J and SN 2002ap, Springer Proc. Phys. 99 (2005) 59–69. arXiv:astro-ph/0404267, doi:10.1007/3-540-26633-X_8.

[21] V. A. Villar, et al., Spitzer Space Telescope Infrared Observations of the Binary Neutron Star Merger GW170817 (2018). arXiv:1805.08192.

[22] M. S. Longair, High-energy astrophysics. Vol. 2: Stars, the galaxy and the interstellar medium, Cambridge University Press, 1994.

[23] H. Abdalla, et al., TeV gamma-ray observations of the binary neutron star merger GW170817 with H.E.S.S, Astrophys. J. 850 (2) (2017) L22. arXiv:1710.05862, doi:10.3847/2041-8213/aa97d2.

[24] R. J. Gould, G. P. Schreder, Pair Production in Photon-Photon Collisions, Phys. Rev. 155 (1967) 1404–1407. doi:10.1103/PhysRev.155.1404.

[25] D. Biehl, D. Boncioli, A. Fedynitch, W. Winter, Cosmic-Ray and Neutrino Emission from Gamma-Ray Bursts with a Nuclear Cascade, Astron. Astrophys. 611 (2018) A101. arXiv:1705.08909, doi:10.1051/0004-6361/201731337.

[26] X. Rodrigues, A. Fedynitch, S. Gao, D. Boncioli, W. Winter, Neutrinos and Ultra-High-Energy Cosmic-Ray Nuclei from Blazars, Astrophys. J. 854 (1) (2018) 54. arXiv:1711.02091, doi:10.3847/1538-4357/aaa7ee.

[27] A. Y. Neronov, D. V. Semikoz, I. I. Tkachev, Ultra-High Energy Cosmic Ray production in the polar cap regions of black hole magnetospheres, New J. Phys. 11 (2009) 065015. arXiv:0712.1737, doi:10.1088/1367-2630/11/6/065015.

[28] K. Murase, J. F. Beacom, Very-High-Energy Gamma-Ray Signal from Nuclear Photodisintegration as a Probe of Extragalactic Sources of Ultrahigh-Energy Nuclei, Phys. Rev. D82 (2010) 043008. arXiv:1002.3980, doi:10.1103/PhysRevD.82.043008.

[29] F. Aharonian, A. M. Taylor, Limitations on the Photo-disintegration Process as a Source of VHE Photons, Astropart. Phys. 34 (2010) 258–266. arXiv:1005.3230, doi:10.1016/j.astropartphys.2010.08.004.

[30] T. K. Gaisser, T. Stanev, S. Tilav, Cosmic Ray Energy Spectrum from Measurements of Air Showers, Front. Phys.(Beijing) 8 (2013) 748–758. arXiv:1303.3565, doi:10.1007/s11467-013-0319-7.

[31] E. Waxman, Cosmological origin for cosmic rays above 10**19-eV, Astrophys. J. 452 (1995) L1–L4. arXiv:astro-ph/9508037, doi:10.1086/309715.

[32] R. Margutti, et al., The Binary Neutron Star Event LIGO/Virgo GW170817 160 Days after Merger: Synchrotron Emission across the Electromagnetic Spectrum, Astrophys. J. 856 (1) (2018) L18. arXiv:1801.03531, doi:10.3847/2041-8213/aab2ad.

[33] A. Albert, et al., Search for High-energy Neutrinos from Binary Neutron Star Merger GW170817 with ANTARES, IceCube, and the Pierre Auger Observatory, Astrophys. J. 850 (2) (2017) L35. arXiv:1710.05839, doi:10.3847/2041-8213/aa9aed.

[34] K. Fang, B. D. Metzger, High-Energy Neutrinos from Millisecond Magnetars formed from the Merger of Binary Neutron Stars, Astrophys. J. 849 (2) (2017) 153, [Astrophys. J.849,153(2017)]. arXiv:1707.04263, doi:10.3847/1538-4357/aa8b6a.

[35] S. S. Kimura, K. Murase, P. Mészáros, K. Kiuchi, High-Energy Neutrino Emission from Short Gamma-Ray Bursts: Prospects for Coincident Detection with Gravitational Waves, Astrophys. J. 848 (1) (2017) L4. arXiv:1708.07075, doi:10.3847/2041-8213/aa8d14.

[36] L. A. Anchordoqui, D. Hooper, S. Sarkar, A. M. Taylor, High-energy neutrinos from astrophysical accelerators of cosmic ray nuclei, Astropart. Phys. 29 (2008) 1–13. arXiv:astro-ph/0703001, doi:10.1016/j.astropartphys.2007.10.006.

[37] R. Aloisio, V. Berezinsky, P. Blasi, Ultra high energy cosmic rays: implications of Auger data for source spectra and chemical composition, JCAP 1410 (10) (2014) 020. arXiv:1312.7459, doi:10.1088/1475-7516/2014/10/020.

[38] N. Globus, D. Allard, R. Mochkovitch, E. Parizot, UHECR acceleration at GRB internal shocks, Mon. Not. Roy. Astron. Soc. 451 (1) (2015) 751–790. arXiv:1409.1271, doi:10.1093/mnras/stv893.

[39] M. Unger, G. R. Farrar, L. A. Anchordoqui, Origin of the ankle in the ultrahigh energy cosmic ray spectrum, and of the extragalactic protons below it, Phys. Rev. D92 (12) (2015) 123001. arXiv:1505.02153, doi:10.1103/PhysRevD.92.123001.

[40] A. Aab, et al., Combined fit of spectrum and composition data as measured by the Pierre Auger Observatory, JCAP 1704 (04) (2017) 038, [Erratum: JCAP1803,no.03,E02(2018)]. arXiv:1612.07155, doi:10.1088/1475-7516/2018/03/E02,10.1088/1475-7516/2017/04/038.

[41] A. Aab, et al., Inferences on mass composition and tests of hadronic interactions from 0.3 to 100 EeV using the water-Cherenkov detectors of the Pierre Auger Observatory, Phys. Rev. D96 (12) (2017) 122003. arXiv:1710.07249, doi:10.1103/PhysRevD.96.122003.